

Article

# Estimation of Grassland Canopy Height and Aboveground Biomass at the Quadrat Scale Using Unmanned Aerial Vehicle

Huifang Zhang<sup>1,2</sup>, Yi Sun<sup>2</sup>, Li Chang<sup>2,3</sup>, Yu Qin<sup>2</sup>, Jianjun Chen<sup>4</sup>, Yan Qin<sup>2,5</sup>, Jiaxing Du<sup>2,5</sup>, Shuhua Yi<sup>1,2,\*</sup>  and Yingli Wang<sup>1</sup>

<sup>1</sup> School of Geographic Sciences, Nantong University, 999 Tongjing Road, Nantong 226007, China; zhf10658@ntu.edu.cn (H.Z.); wyl621021@ntu.edu.cn (Y.W.)

<sup>2</sup> State Key Laboratory of Cryospheric Sciences, Northwest Institute of Eco-Environment and Resources, Chinese Academy of Sciences, 320 Donggang West Road, Lanzhou 730000, China; sunyi@lzb.ac.cn (Y.S.); changli2012@lzb.ac.cn (L.C.); qiny@lzb.ac.cn (Yu.Q.); qyan@lzb.ac.cn (Ya.Q.); dujx@lzb.ac.cn (J.D.)

<sup>3</sup> State Key Laboratory Breeding Base of Desertification and Aeolian Sand Disaster Combating, Gansu Desert Control Research Institute, 390 North Bank Road West, Lanzhou 730070, China

<sup>4</sup> College of Geomatics and Geoinformation, Guilin University of Technology, 12 Jiangan Road, Guilin 541004, China; chenjj@glut.edu.cn

<sup>5</sup> University of Chinese Academy Sciences, Beijing 100049, China

\* Correspondence: yis@lzb.ac.cn; Tel.: +86-931-496-7356

Received: 13 April 2018; Accepted: 28 May 2018; Published: 31 May 2018



**Abstract:** Aboveground biomass is a key indicator of a grassland ecosystem. Accurate estimation from remote sensing is important for understanding the response of grasslands to climate change and disturbance at a large scale. However, the precision of remote sensing inversion is limited by a lack in the ground truth and scale mismatch with satellite data. In this study, we first tried to establish a grassland aboveground biomass estimation model at 1 m<sup>2</sup> quadrat scale by conducting synchronous experiments of unmanned aerial vehicle (UAV) and field measurement in three different grassland ecosystems. Two flight modes (the new QUADRAT mode and the commonly used MOSAIC mode) were used to generate point clouds for further processing. Canopy height metrics of each quadrat were then calculated using the canopy height model (CHM). Correlation analysis showed that the mean of the canopy height model (CHM\_mean) had a significant linear relationship with field height ( $R^2 = 0.90$ , root mean square error (RMSE) = 19.79 cm, rRMSE = 16.5%,  $p < 0.001$ ) and a logarithmic relationship with field aboveground biomass ( $R^2 = 0.89$ , RMSE = 91.48 g/m<sup>2</sup>, rRMSE = 16.11%,  $p < 0.001$ ). We concluded our study by conducting a preliminary application of estimation of the aboveground biomass at a plot scale by jointly using UAV and the constructed 1 m<sup>2</sup> quadrat scale estimation model. Our results confirmed that UAV could be used to collect large quantities of ground truths and bridge the scales between ground truth and remote sensing pixels, which were helpful in improving the accuracy of remote sensing inversion of grassland aboveground biomass.

**Keywords:** vegetation height; grassland; aboveground biomass; UAV; canopy height model; structure from motion (SfM); FragMAP

## 1. Introduction

Grassland ecosystems are an important component of natural ecosystems, accounting for 15% of Earth's surface area [1]. They not only provide food and habitat for herbivores [2], but also play an important role in environmental protection, such as water conservation, sand fixation, and soil conservation [3,4]. In addition, grassland ecosystems play a critical role in the global carbon cycle and

in climate regulation [5,6]. Compared with other ecosystems, grassland ecosystems are more vulnerable to climate change [7]. Biomass is one of the important indicators for evaluating grassland ecosystems. Studies have shown that it is highly susceptible to meteorological factors, such as temperature, precipitation, and surface temperature. In addition, variable biomass-climatic relationships exist within different grassland ecosystems [8–10]. Therefore, an accurate estimation of grassland biomass would significantly increase our understanding of the response of grasslands to climate change and disturbance, and the coupling mechanism of grassland ecosystems and climate change.

Remote sensing has recently become a major data source for estimating biomass over large areas. For example, different remote sensing data have been used to extract grassland biomass information, such as IKONOS images with 1 m spatial resolution [11], Landsat, and SPOT data with 30 m and 20 m spatial resolution, respectively [12–18], the moderate resolution imaging spectroradiometer (MODIS) and the advanced very high resolution radiometer (AVHRR) data with 1 km spatial resolution [8,19–24], or hyperspectral remote sensing data [25,26]. Regardless of the type of spatial resolution satellite data used for estimating grassland biomass, it is essential that relationships between field biomass measurements and corresponding spectral indices obtained by satellite be established. Thus, the quantity and quality of field-scale grassland biomass samples are important factors for influencing the accuracy of biomass inversion.

Field-scale biomass is typically collected by methods of destructive sampling, calibrated visual estimation, and proximal sensing measurements with spectrometers [27–31]. Common shortcomings exist among these methods which are time-consuming and labor intensive, thus, it is difficult to acquire vegetation biomass at large scales. In addition, it is impossible to collect all the grassland biomass information within a satellite pixel for constructing the biomass estimation model. A more rational method is to set 3 to 5 quadrats in a pixel, and then average the sampling points to estimate the pixel grassland biomass [16,32–36]. As a result, spatial scale mismatching occurs between ground-based observation data and satellite data. Therefore, increasing the sample sizes of ground truth and resolving the scale mismatch issues are of great significance to improve the accuracy of grassland biomass estimation.

The emergence of the unmanned aerial vehicles (UAV) has made it possible to solve these two problems. As a new technology, UAV has shown potential for estimation of terrestrial vegetation biomass [37–39]. Compared with satellite remote sensing data, its flight mode is more flexible. The flight height of UAV ranges from a few meters to hundreds of meters, and its shooting angle can be adaptable for different applications. UAV equipped with a laser system can invert the vegetation information. For example, UAV-Lidar systems have been used to estimate the biomass of forest [40,41], crop [42], and grassland [43,44]. However, due to the high cost of acquiring LIDAR data, studies were mostly limited to small areas and have not been widely applied in large areas.

In addition, UAV with an optical camera has been used to accurately estimate vegetation biophysical characteristics, such as canopy height, vertical structure using a combination of structure from motion (SfM) algorithm, and a canopy height model (CHM) [37,38,45,46], which can be used to improve the accuracy of biomass estimation. The SfM is a computer technique that can generate 3D geometry by automatically extracting the corresponding feature points from unordered overlapped UAV RGB images and optimizing the 3D location of corresponding features based on the principles of photogrammetry [47]. The CHM is one of the most common methodologies designed to extract the vegetation canopy height parameter from point clouds. These technologies have been primarily used to estimate biomass of forest [48–50], shrub [51,52], and crop [37,38,46,53]. However, the accuracy of inversion results of the CHM algorithm is closely related to the number of point clouds. When the quality of the generated point cloud data is insufficient for distinguishing the ground and vegetation point clouds, the algorithm cannot accurately invert the vegetation height information. As a result, few studies have been conducted over grassland [29,54] and wetland [55], since the height of herbage is much smaller than that of forest and shrub.

In this study, we focused on the development of a novel method for estimating the quadrat-scale aboveground biomass of low-stature vegetation. We first introduced a new non-destructive method to estimate the grassland canopy height and aboveground biomass by using SfM and CHM algorithms from UAV RGB images at quadrat scale. We then established and tested the relationships between canopy height and biomass using in situ measurements. Finally, we applied the established quadrat-scale relationships to estimate grassland aboveground biomass in a large plot area.

## 2. Materials and Methods

### 2.1. Study Sites

To evaluate the performance of the inversion of grassland canopy height and aboveground biomass by using aerial photographs of UAV, three different study sites were selected from the Gansu, Inner Mongolia, and Jiangsu provinces of China (Figure 1).

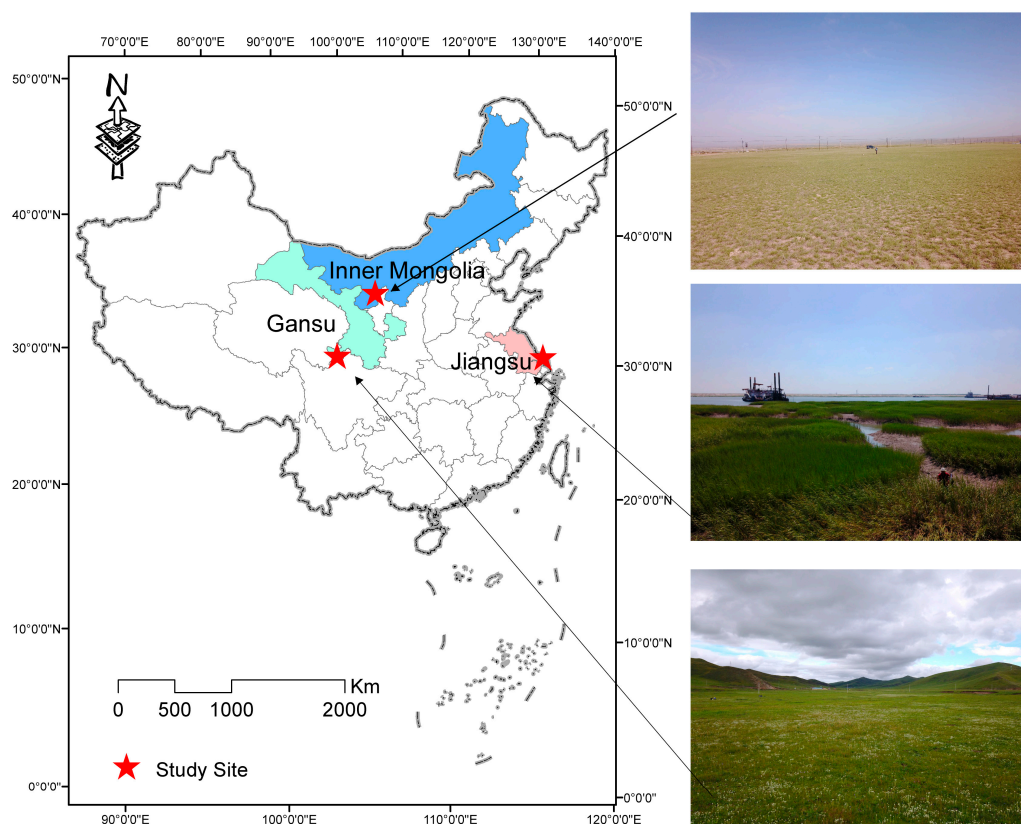


**Figure 1.** The location of study sites.

The Gansu study site is located in Maqu County of Gansu Province, located in the eastern section of the Qinghai-Tibet Plateau. Annual temperature and precipitation rates averaged 2 °C and 600 mm, respectively. During the growing season (May to August), the average temperature and precipitation rates were recorded at 10.4 °C and 400 mm, respectively, whereas during the cold season (September to April), they averaged −1.5 °C and 200 mm, respectively. The duration of sunlight at this site is approximately 2580 h with more than 270 days of frost per year. The primary vegetation type in this site is alpine meadow, for example, Poaceae and Cyperaceae [56].

The Inner Mongolia study site is located in Alashanzuoqi County of the Inner Mongolia autonomous region. The area is a temperate desert arid region exhibiting a typical continental climate. The average annual rainfall ranges from 80 mm to 220 mm, with an annual evaporation of 2900~3300 mm. The site experiences 3316 h of sunlight, an annual average temperature of approximately

7.2 °C, and a frost-free period of 120 to 180 days. The typical grassland types of this region are primarily desert and semi-desert steppe, such as *Stipa glareosa*, *Iris lactea* Pall. var. *chinensis* (Fisch.) Koidz, and *Bassia dasyphylla*.

The Jiangsu study site has a northern subtropical monsoon climate, with a mean annual temperature of  $-1.5\sim 2.5$  °C in winter and  $26.5\sim 27.5$  °C in summer, and an annual precipitation range from 850 to 1000 mm. The grassland type in this area belongs to salt marsh, with plant species such as *Spartina alterniflora*, *Suaeda glauca* Bunge, and *Phragmites australis*.

## 2.2. Methods

A flowchart for estimation of grassland canopy height and aboveground biomass at 1 m<sup>2</sup> quadrat scale is shown in Figure 2, summarized in four steps: (1) acquire UAV photos; (2) generate dense point clouds; (3) calculate canopy height model (CHM); and (4) establish vegetation height and aboveground biomass estimation models. More detailed information is described in the following sections.

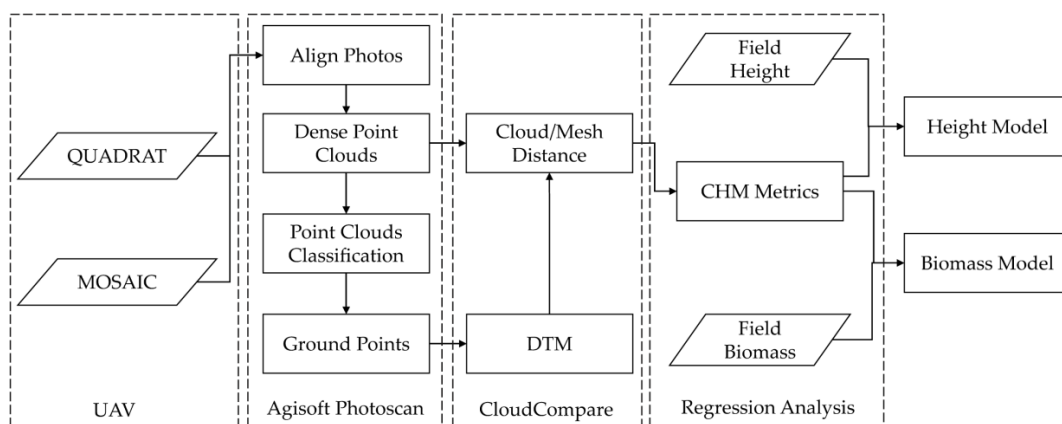


**Figure 2.** The flowchart of estimation of grassland canopy height and aboveground biomass.

### 2.2.1. UAV System and Flight Modes

DJI Phantom3 Professional (DJI-Innovations, Shenzhen, China) was used for field observation in this study. It is a lightweight four-wheel UAV with an integrated 4k camera. The camera featured a 94° angle-of-view lens with an f/2.8 aperture, and a maximum picture size of 4000 × 3000 pixels. More detailed parameters are included in Table 1. The maximum flight altitude is 6000 m above sea level, and the working temperature ranges from 0 °C to 40 °C. In order to obtain a more precise flight position, this UAV is equipped with an inertial measurement unit and GPS/GLONASS, with a GPS accuracy of 1.0 m in the horizontal direction. In addition, the DJI Innovation Company provides a software development kit (SDK) for developers, making it possible to design a specific flight route and flight height for a certain purpose.

**Table 1.** The detailed parameters of the camera of DJI phantom3 Professional.

Parameter	Value	Parameter	Value
image sensor	1/2.3 inch CMOS	RGB color space	sRGB
camera lens	FOV 94° 20 mm	shutter speed	1/8000 s
aperture	f/2.8	photo size	4000 × 3000 pixels
ISO range	100–1600	image format	JPEG

The FragMAP software (version 4.2) [57–59] has been used in the past to accomplish the automatic flight of the UAV rather than manual operation, reduce the probability of mistakes due to improper manual operation, and improve the efficiency of image acquisition.

A new QUADRAT flight mode was designed to obtain vegetation point clouds at quadrat scale. Its flight routes were planned as follows: (1) the FragMAP first generated five sample quadrats evenly according to the predefined size, for example, 30 m  $\times$  30 m (Figure 3a). The location of these quadrats could be further adjusted to meet actual situational needs. (2) The UAV flew to the center of each quadrat to take four photos vertically at a 90-degree interval. (3) The UAV then flew to a distance of 2 m from the quadrat center and took 3 pictures toward the center at 45-degree intervals;  $\theta$  was 15° (Figure 3b). Owing to the error of GPS, the flight trajectory of each quadrat would be slightly different, especially in a small area (Figure 3a). In this study, the height of the QUADRAT flight mode was 3 m to ensure grassland with low height could be clearly seen in the UAV images.

The commonly used MOSAIC flight mode was also used in this study [57]. Since the scene captured by lightweight UAV was limited, it was impossible to obtain a large plot area (for example,  $\sim$ 180 m  $\times$  160 m) in one shot at low altitude. In fact, it often required hundreds of overlapping photographs stitched together capture a picture of the entire area [60]. As a result, the MOSAIC mode was developed to align the proper flight path to ensure the overlap rate of UAV photos was no less than 70% along and parallel to the flying direction (Figure 4). The height and flying speed of UAV were set to 20 m and 2 m/s, respectively, and the camera was set to a vertically downward direction.

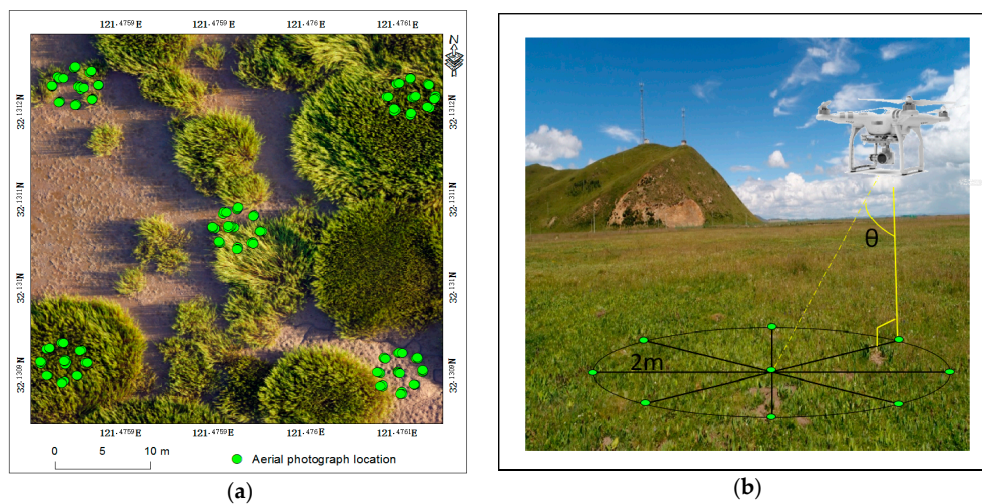


**Figure 3.** The unmanned aerial vehicle (UAV) flight trajectory of the QUADRAT flight mode (a); and the UAV shooting mode diagram for each quadrat (b); (the solid green dots are locations of aerial photographs).

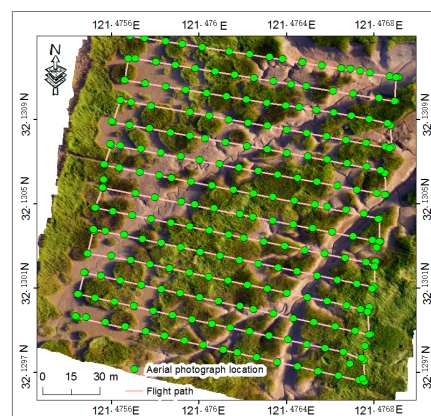


**Figure 4.** The UAV flight trajectory of the MOSAIC flight mode. The solid green dots are the locations of aerial photographs. The pink line is the flight trajectory of the UAV.

### 2.2.2. Synchronous Experiments of UAV and Field Measurements

To evaluate the performance of UAV in retrieving vegetation aboveground biomass at quadrat scale, the synchronous experiments of UAV and field measurements were conducted at each study site in August 2017. Twenty  $30\text{ m} \times 30\text{ m}$  plots were set up at each site (8, 4, and 8 in the Gansu, Inner Mongolia, and Jiangsu sites, respectively) with 3–5 quadrats in each plot, totalling 75. One frame was placed in each quadrat (Figure 5). Due to the healthy herb growth and even distribution in the Gansu study area, a  $0.5\text{ m} \times 0.5\text{ m}$  sample frame was used to collect the grassland aboveground biomass. Alternatively, the fractional vegetation cover in the Inner Mongolia site was not as good, and thus a  $1\text{ m} \times 1\text{ m}$  sample frame was used. In the Jiangsu site, the average height of grassland was approximately 1.5 m, much higher than in the other two sites, thus a  $1\text{ m} \times 1\text{ m}$  sample frame was used to ensure it could be seen clearly in the UAV images. Aerial photographs for each plot were acquired using the FragMAP software with the QUADRAT and MOSAIC flight modes. Field measurements were conducted immediately after the UAV flights. To ensure that the average height of vegetation within each frame was calculated accurately, a stratified random sampling strategy was used. In each frame, the vegetation was roughly divided into three categories: high, medium, and low according to the relative height of vegetation. Vegetation height was measured five times for each category. The average canopy height of each frame was calculated and referred to as Field Height (Fd\_Height). Thereafter, aboveground vegetation in the frame was harvested and dried at  $65\text{ }^\circ\text{C}$  to calculate the dry aboveground biomass per frame, referred to as Field Biomass (Fd\_Biomass ( $\text{g}/\text{m}^2$ )). A total of 75 destructive aboveground biomass samples were collected.

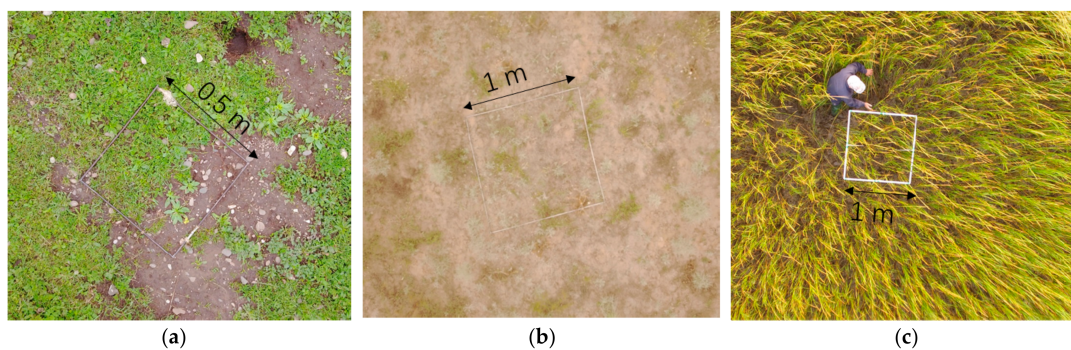


**Figure 5.** A quadrat with frame in the Gansu (a), Inner Mongolia (b), and Jiangsu study sites (c).

### 2.2.3. Point Cloud Generation and Classification

After aerial photographing and field measurements, the SfM algorithm was employed to generate point clouds for each quadrat to obtain the 3D structure metrics of vegetation. Agisoft PhotoScan software (Agisoft LLC, St. Petersburg, Russia, version 1.3.0) was chosen to perform the SfM algorithm for its user-friendly interface and high-efficiency operation performance [61,62], accomplished using three processes. (1) Add photos: 28 overlapped photos were added for each quadrat for computing. (2) Align photos: Agisoft Photoscan was used to align images by calculating the position and orientation of each photo and to build a sparse point cloud model. In this step, the parameter of accuracy was set to high and photos with poor resolution were removed. Incorrectly positioned photos with greater errors were subsequently removed by using the returning error analysis results from the Agisoft software to ensure high quality generation of sparse cloud points. (3) Build dense clouds: the depth information for each camera was calculated based on the estimated camera positions and then combined together to generate dense point clouds for each quadrat. The parameters of quality and depth filtering were set as high and aggressive, respectively. All dense point clouds were produced with high quality to obtain more accurate geometry of vegetation 3D structure metrics.

After completing the above steps, dense point clouds were further divided into both ground point and non-ground point clouds by using the following algorithms. There were two point clouds classification options in the Agisoft PhotoScan program: one with an automatic division of all the points into the two classes of ground and non-ground points, and the second with a manual classification [62]. These two methods were used together in this study to identify the ground points. The automatic classification procedure consisted of two steps. The first step was to divide dense point clouds into cells of a certain size. In each cell, the lowest point was detected to generate the first approximate mesh of the terrain model. The second step was to calculate the distance and angle between the terrain model and the new point whenever a new point was added. If the value of distance or angle was less than a certain threshold, the new point would be classified as a ground point; otherwise as a non-ground point. A new triangulation of a terrain model would then be updated by including this new point. The second step was repeated until all points were checked [62]. Due to the flat terrain of the study area, the maximum angle and the maximum distance were set to  $15^\circ$  and 0.001 cm, respectively. The cell size was set to 0.1 m owing to the small coverage area of the generated point cloud, that is, about  $5\text{ m} \times 6\text{ m}$ . In addition to the automatic classification of the ground method, Agisoft PhotoScan allows users to associate all points within dense clouds with a certain standard class, such as ground, building, vegetation, and water, to meet the classification needs [62]. Given the significant color difference in bare ground and vegetation, we also identified ground points by using RGB attributes of point clouds. Since the bare ground of different study sites showed different colors in aerial photos, the color threshold was adjusted for each quadrat to ensure ground points could be selected with high accuracy.

#### 2.2.4. Digital Terrain Models (DTM)

Digital Terrain Models for each site were generated from ground point clouds by using the creating mesh function of CloudCompare software (version 2.8.1). CloudCompare is a 3D point cloud and triangular mesh processing software [63]. It was designed to perform a comparison between two dense 3D point clouds or between a point cloud and a triangular mesh. When compared with Agisoft Photoscan software, CloudCompare was a more generic point cloud processing software given its many advanced algorithms, such as registration between two point clouds, resampling the point cloud, interactive segment, and static computing, which had critical functions for point cloud computing. Hence, dense point clouds in each quadrat and their corresponding classified ground points were exported into CloudCompare for subsequent processing.

#### 2.2.5. Canopy Height Models and CHM Metrics

Canopy height models (CHM) were generated by computing the distances between dense point clouds and their corresponding ground meshes using the cloud/mesh distance function. In this algorithm, the model searched for the nearest triangular in the reference mesh for each point of the compared point cloud to compute the distance. To accurately compare the point clouds retrieved from UAV with field sample data, generated point clouds were cut by using the segment function and thus only the point clouds in the frame were retained for further calculation (Figure 6a). The CHM height metrics were then calculated within each frame at a height  $>0\text{ m}$ , including the median (CHM\_median), mean (CHM\_mean), minimum (CHM\_min), maximum (CHM\_max), and standard deviation (CHM\_sd). The vegetation coverage index of each quadrat was extracted using FragMAP software [57] (Figure 6b), which identified the green vegetation by using the excess green index (EGI) [64]:  $EGI = 2G - R - B$ , where R, G, and B represent the 0–255 value at the red, green, and blue bands, respectively. To evaluate whether the vegetation cover had an impact on aboveground biomass estimation, we also calculated the average height of the point clouds belonging to the vegetation type in each quadrat, defined as the variable CHM\_height\_green.

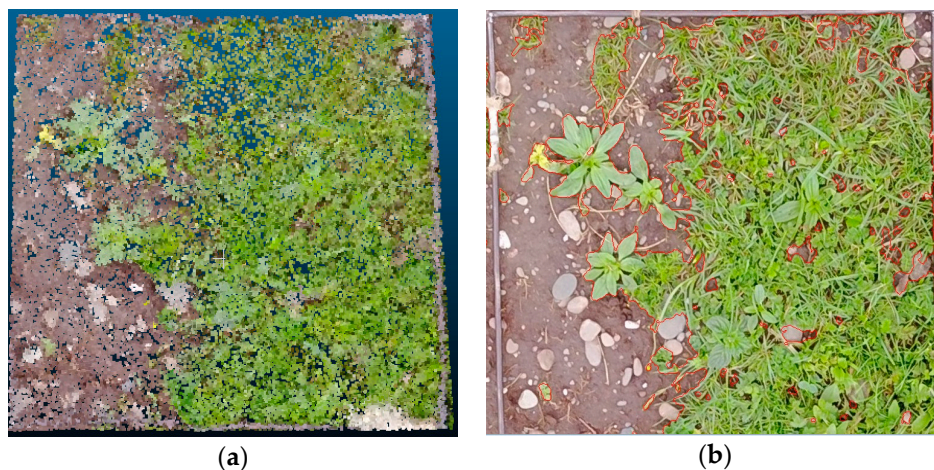


**Figure 6.** The point clouds of a frame in one quadrat in the Gansu study site (a); and the corresponding vegetation extraction result (b).

### 2.2.6. Aboveground Biomass Estimation Model

Aboveground biomass models were generated by establishing the relationship between CHM metrics and field measured aboveground biomass using R statistics software (version 3.4.2). When constructing the model, 70% of the samples were randomly selected as the training data and the remaining 30% as the independent validation data. The coefficients of determination ( $R^2$ ), root mean square error (RMSE), and relative root mean square error (rRMSE) indices were used to quantify the fitting accuracy of the constructed models.

## 3. Results

### 3.1. Correlation of CHM Metrics and Field Measurements Analysis

Point clouds of quadrat scale were successfully generated from UAV photos of QUADRAT mode in the Gansu and Inner Mongolia sites, and from MOSAIC mode in the Jiangsu site. Therefore, we only used successfully generated point clouds for further analysis. Prior to construction of the aboveground biomass estimation model, the correlations between the canopy height metrics and field measured indices were analyzed at quadrat scale. The mean height of field heights (Fd\_Height) was significantly correlated with the CHM\_mean ( $r = 0.95$ ), CHM\_median ( $r = 0.94$ ), CHM\_max ( $r = 0.95$ ), and CHM\_height\_green ( $r = 0.94$ ) metrics obtained from UAV inversion (Figure 7). Aboveground biomass had positive correlations with the CHM\_mean ( $r = 0.86$ ) and the CHM\_max ( $r = 0.87$ ), but had a relatively lower correlation with CHM\_height\_green ( $r = 0.83$ ). Strong correlations were also found among CHM\_mean, the CHM\_max, CHM\_median, and CHM\_height\_green. The correlation analysis showed that CHM metrics obtained from UAV were well correlated with field measurements, which could be used to retrieve the canopy height and aboveground biomass of grassland.

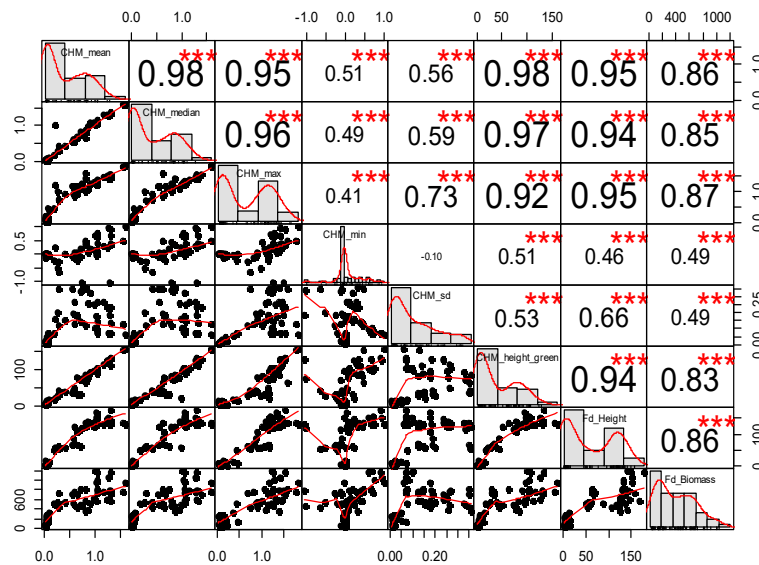


**Figure 7.** The correlation coefficient charts between canopy height model (CHM) metrics and field measurement for all three study sites. The diagonal line in the figure shows the distributions of the variables themselves. The lower triangle (left and the bottom of the diagonal) in the figure shows scatter plots of the two properties. The upper triangle (upper right of the diagonal) in the figure indicates the correlation values of the two attributes; the asterisk indicates the degree of significance (more stars indicate greater significance, \*\*\* =  $p$ -value of  $<0.001$ ). The bold bigger numbers mean the higher correlation.

### 3.2. Vegetation Height Estimation Model

As shown in Figure 7, Fd\_Height had a significant correlation with CHM\_max, CHM\_mean, CHM\_median, and CHM\_height\_green indices ( $p < 0.001$ ). However, scatter plots between Fd\_Height and these indices indicated that Fd\_Height had a better fit with CHM\_mean and CHM\_height\_green indices (Figure 7). Therefore, we conducted a comparative test between these two indices with results showing no significant differences between the two indices (Table 2). The  $R^2$  between the CHM\_mean and Fd\_Height was 0.90, and the rRMSE was 16.50%, which was slightly better than that of CHM\_height\_green, and had a good fit with Fd\_Height (Figure 8). These results indicated that vegetation coverage had little effect on the UAV estimation of average vegetation height at quadrat scale. Since the metric CHM\_mean was more accessible than CHM\_height\_green, it was selected to predict the grassland average height at quadrat scale.

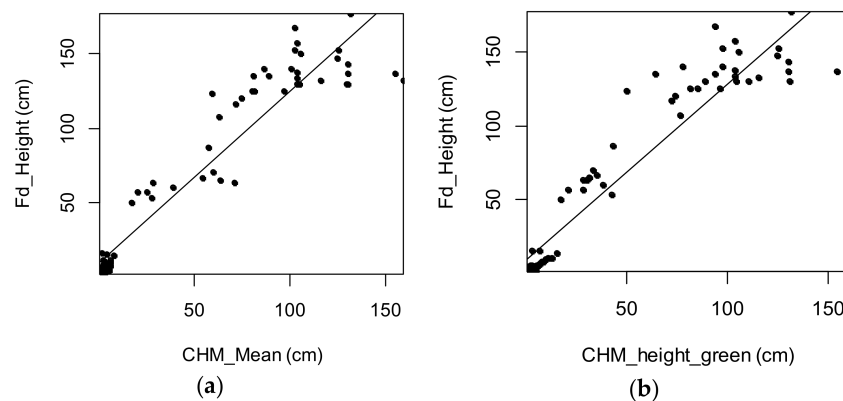


**Figure 8.** The scatter plot of Fd\_Height and CHM\_mean (a); and the scatter plot of Fd\_Height and CHM\_height\_green (b).

**Table 2.** The comparison results between vegetation height models from all 75 samples.

Variable	R <sup>2</sup>	RMSE (cm)	rRMSE (%)
CHM_Mean	0.90	19.79	16.50
CHM_height_green	0.88	20.89	17.42

### 3.3. Aboveground Biomass Estimation Models

Figure 7 showed that the aboveground biomass had a high correlation with the CHM\_mean, CHM\_max, and CHM\_median metrics. Thus, either a linear or a nonlinear regression analysis was performed between Fd\_Biomass and these metrics (Figure 9). The fitting effects of logarithmic models were better than linear models (Table 3). The value of R<sup>2</sup> varied from 0.66 to 0.78. Even though the CHM\_max had the highest correlation with Fd\_Biomass ( $r = 0.87$ ), its fitting accuracy was not the highest. Instead, the CHM\_mean had the highest coefficients of determination (R<sup>2</sup> = 0.78) among all models and with the lowest root mean square error (RMSE = 162.2 g/m<sup>2</sup>, rRMSE = 25.36%). Furthermore, all models were validated by using the independent validation data (Figure 10). It showed that logarithmic models had better fitting accuracy than linear models. Among all three logarithmic (M2, M4, M6) models (Table 4), the CHM\_mean logarithmic model (M4) showed the highest fitting accuracy (R<sup>2</sup> = 0.89, RMSE = 91.48 g/m<sup>2</sup>, rRMSE = 16.11%), followed by CHM\_median and CHM\_max models.

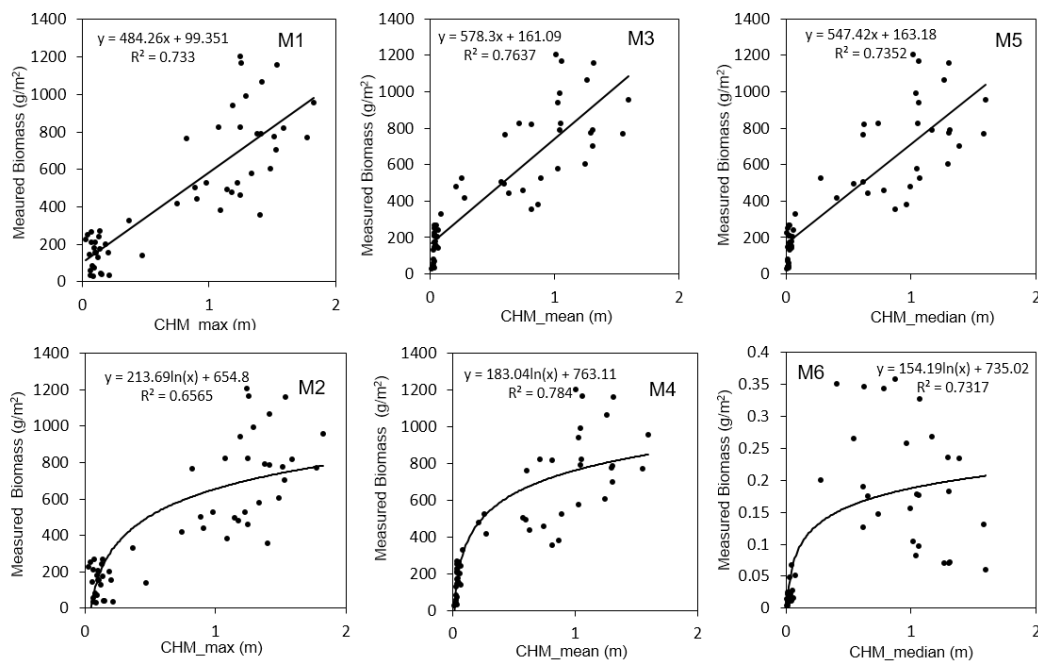


**Figure 9.** The regression graph results of the six different biomass estimation models. M1: the linear regression constructed by CHM\_max; M2: the logarithmic regression constructed by CHM\_max; M3: the linear regression constructed by CHM\_mean; M4: the logarithmic regression constructed by CHM\_mean; M5: the linear regression constructed by CHM\_median; M6: the logarithmic regression constructed by CHM\_median.

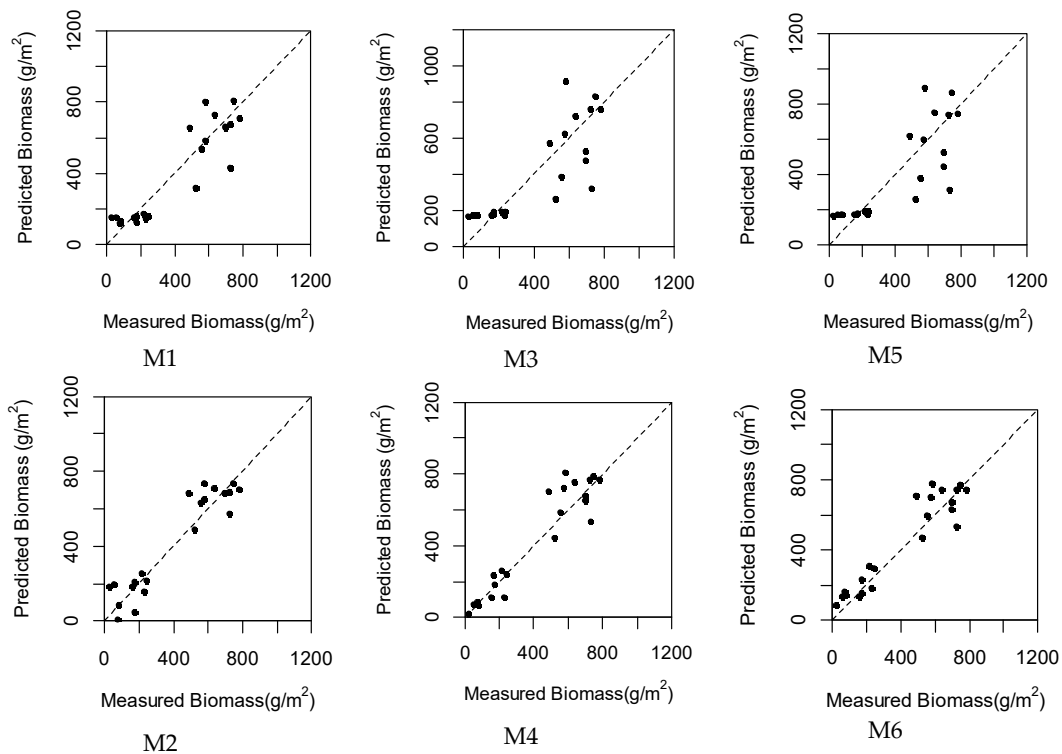


**Figure 10.** The scatter plots of measured and predicted aboveground biomass of six different aboveground biomass estimation models using independent validation data. M1: the linear regression constructed by CHM\_max; M2: the logarithmic regression constructed by CHM\_max; M3: the linear regression constructed by CHM\_mean; M4: the logarithmic regression constructed by CHM\_mean; M5: the linear regression constructed by CHM\_median; M6: the logarithmic regression constructed by CHM\_median.

**Table 3.** The regression results of the six aboveground biomass estimation models. M1: the linear regression constructed by CHM\_max; M2: the logarithmic regression constructed by CHM\_max; M3: the linear regression constructed by CHM\_mean; M4: the logarithmic regression constructed by CHM\_mean; M5: the linear regression constructed by CHM\_median; M6: the logarithmic regression constructed by CHM\_median.

Model	Equation	R <sup>2</sup>	RMSE (g/m <sup>2</sup> )	rRMSE (%)
M1	$484.26 \times \text{CHM\_max} + 99.35$	0.73	180.3	28.19
M2	$213.69 \times \ln(\text{CHM\_max}) + 654.80$	0.66	204.6	31.99
M3	$578 \times \text{CHM\_mean} + 161.09$	0.76	169.7	26.54
M4	$183.04 \times \ln(\text{CHM\_mean}) + 763.11$	0.78	162.2	25.36
M5	$547.42 \times \text{CHM\_median} + 163.18$	0.74	179.6	28.08
M6	$154.19 \times \ln(\text{CHM\_median}) + 735.02$	0.73	180.0	28.15

**Table 4.** The validation results of the six aboveground biomass estimation models. The comparison between predicted aboveground biomass and field measured biomass by using the validation dataset.

Regression Type	Model	R <sup>2</sup>	RMSE (g/m <sup>2</sup> )	rRMSE (%)
linear regression model	M1	0.83	115.4	20.32
	M3	0.67	158.6	27.92
	M5	0.66	162.3	28.57
non-linear logarithmic regression model	M2	0.89	93.47	16.46
	M4	0.89	91.48	16.11
	M6	0.89	93.33	16.43

Therefore, the CHM\_mean logarithmic regression model was the best aboveground biomass estimation model at quadrat scale.

## 4. Discussion

### 4.1. The Flight Modes of Taking Aerial Photos at Quadrat Scale

QUADRAT flight mode was used to collect UAV photographs of grassland at a height of 3 m in all three study sites. It was found that UAV images obtained by QUADRAT flight mode were successfully used to create dense point clouds for each quadrat in two study sites except for the Jiangsu site (Figure 11). This was due to high vegetation coverage and density in the Jiangsu site, and the lack of obvious feature points, such as bare ground, to align photos. Therefore, the commonly used MOSAIC flight mode was utilized instead of the QUADRAT flight mode to obtain vegetation photographs at quadrat scale in the Jiangsu study site.

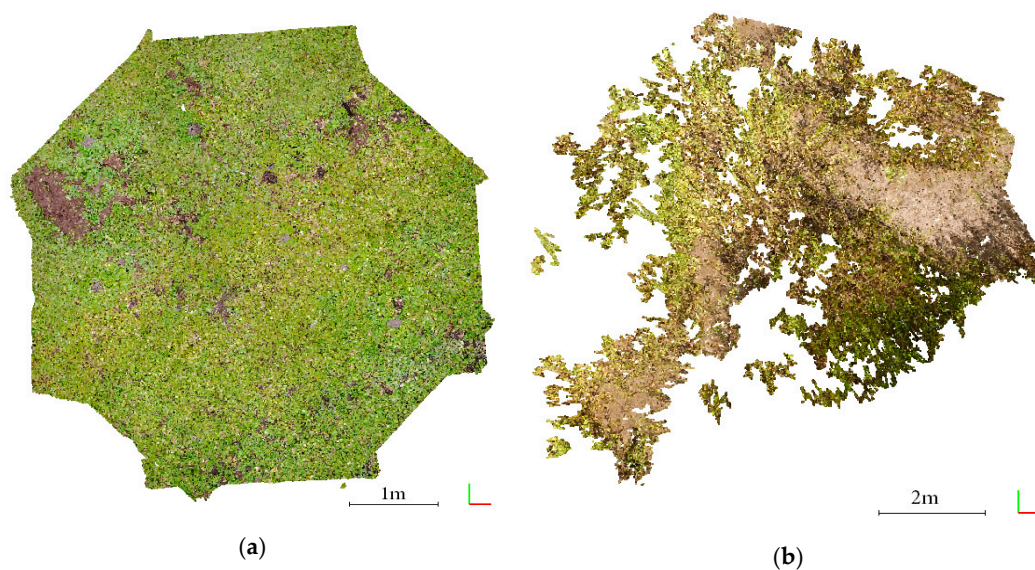


**Figure 11.** Examples of dense point clouds of grassland generated from UAV photos using the QUADRAT flight mode in the Gansu site (a) and Jiangsu site (b).

To ensure high-resolution images for the generated point cloud or orthography in the MOSAIC flight mode, it is critical that the photo overlap ratio be no less than 70% along and parallel to the flight direction. It is well-known that the overlap ratio is also affected by the UAV flight height, flight speed, and shooting interval. After several flight experiments, we found that the generation of *Spartina alterniflora* point clouds could be ensured if flight parameters of the overlap ratio, flight height, flight speed, and shooting interval were set to 70%, 20 m, 2 m/s and 3 s, respectively. We were unable to generate point clouds at the other two sites (results not shown here), thus necessitating the need for further studies to investigate the causes.

### 4.2. The Effects of Grassland Density on the Generation of Point Clouds and DTM

Three different grassland ecosystems were verified for exploring the feasibility of inversion of plant height and aboveground biomass from UAV RGB images. The most critical steps were the generation of dense point clouds and the accurate acquisition of DTM for each quadrat.

During the process, it was found that the quality of generated dense point clouds was not only related to the overlap rate of the acquired UAV photos, but also to the density of the vegetation in the shooting area. If the density of grassland was too high, then the quality of generated point clouds was relatively poor with a certain degree of deformation. Due to the high-density coverage of vegetation,

the SfM algorithm could not automatically extract enough corresponding feature points to determine the correct geometric position of the point cloud. As a result, additional marker points were added by visualization to improve the quality point clouds, yet, in the occurrence of greater grassland density, there was no obvious improvement in quality. Thus, the use of QUADRAT mode to obtain point clouds failed in the Jiangsu study site (Figure 11b). However, quantitative analysis of the influence of grassland density on the quality of point clouds had not yet been conducted. In future research, the polygon grids method will be utilized to further quantify the impact of vegetation density on the quality of point clouds [65].

The quality of DTM was also influenced by the density of grassland. If the vegetation density was moderate, the extraction of ground points was relatively easy, but if the density was too high, an accurate DTM could not be generated due to insufficient ground points. In this step, we not only used the automatic ground point classification provided by Agisoft Photoscan, but also the RGB attributes to identify the ground point cloud, since RGB information was useful for distinguishing or monitoring the grassland [66].

#### 4.3. Estimation of Grassland Canopy Height from UAV

Our results indicated that the CHM\_mean significantly correlated with field measured canopy height at quadrat scale (Table 2), which further confirmed that grassland canopy height can be retrieved by UAVs. In contrast to forest or shrub, grassland has a low vegetation height. For example, vegetation height in the Jiangsu site was less than 2 m, and the height observed in the Inner Mongolia and Gansu sites was even lower, typically less than 50 cm. Inconsistent with the previous study [67], our results indicated that CHM could also be used to infer the height of short vegetation with high accuracy. It was reported that CHM\_mean was the most suitable variable for estimating ground vegetation height [37,45]. Our results also fit this pattern. It was also found that CHM\_mean canopy height of grassland was usually lower than the field measured height [37]. The possible causes for this phenomenon are as follows: (1) the number of plant height measurement was small, and the mean field measurement height did not represent the true average vegetation height at quadrat scale; and (2) the field canopy height was measured as the vertical distance between the top of vegetation and ground surface. However, the dense cloud points generated by UAV could capture the entire height information of grassland, including the stem, but not the top of the vegetation. Consequently, inverted average vegetation height was always lower than measured mean canopy height, which was comparable to the results obtained using airborne lidar system [68,69].

#### 4.4. Error Analysis of the Predicted Aboveground Biomass

The predicted errors of aboveground biomass were calculated to evaluate the performance of UAV at quadrat scale by using the independent validation dataset. The aboveground biomass error estimation differed for all three study sites (Figure 12a). The Jiangsu site had the largest error ranging from 9.34 to  $-233.45 \text{ g/m}^2$ , the RMSE was  $125.6 \text{ g/m}^2$ , and the rRMSE was 19.55% (Table 5). At the Gansu site, the RMSE and rRMSE of predicted biomass were  $34.35 \text{ g/m}^2$  and 22.11%, respectively (Table 5). Although the Inner Mongolia site had the smallest RMSE (RMSE =  $16.19 \text{ g/m}^2$ ), the rRMSE was the largest among the three sites (rRMSE = 43.92%). This could be attributed to the low aboveground biomass in Inner Mongolia. The average biomass in Inner Mongolia was only  $36.87 \text{ g/m}^2$  (Table 5), which was significantly smaller than the other two study sites. The predicted percentage errors were typically 25% (Figure 12b). Our results were consistent with previous studies, which reported the mean relative error of a grassland aboveground biomass estimation model, using random forest algorithm, was 28% [70].

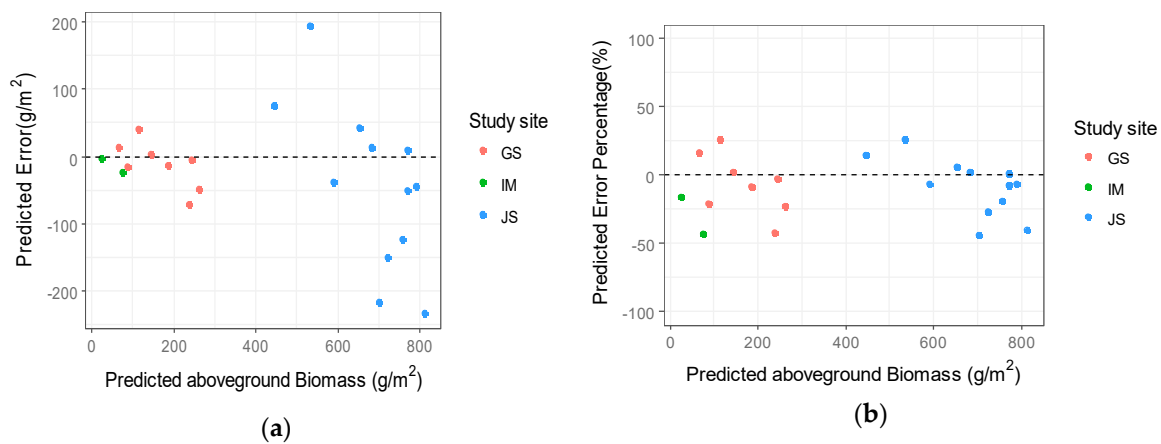


**Figure 12.** The scatter plots of predicted aboveground biomass and estimation error at quadrat scale (a) and the scatter plot of predicted biomass error percentage of different study sites (b). GS: Gansu study site; IM: Inner Mongolia study site; JS: Jiangsu study site.

**Table 5.** The errors of predicted aboveground biomass at different sites.

Study Site	Error_Min ( $\text{g/m}^2$ )	Error_Max ( $\text{g/m}^2$ )	Mean_Biomass ( $\text{g/m}^2$ )	RMSE ( $\text{g/m}^2$ )	rRMSE (%)
Gansu	2.98	70.72	155.4	34.35	22.11
Inner Mongolia	−3.42	−22.64	36.87	16.19	43.92
Jiangsu	9.34	−233.45	642.29	125.60	19.55

#### 4.5. Estimation of Grassland Aboveground Biomass at Plot Scale

A preliminary experiment was conducted at the Jiangsu site to estimate the grassland aboveground biomass at a plot scale ( $180 \text{ m} \times 160 \text{ m}$ ) by jointly using UAV and the constructed  $1 \text{ m}^2$  quadrat aboveground biomass estimation model. For this purpose, overlapped UAV images were first obtained from the MOSAIC mode. A grassland height map with  $\sim 1 \text{ cm}$  spatial resolution was then generated from these images by using SfM and CHM algorithms and were resampled into a  $1 \text{ m}$  spatial resolution. It should be noted that during the resampling, the new pixel values were recalculated as the mean value of the original pixels that fell within the range of  $1 \text{ m} \times 1 \text{ m}$ . Subsequently, the quadrat scale estimation models were applied over each  $1 \text{ m} \times 1 \text{ m}$  pixel to calculate the aboveground biomass over the entire plot.

The results showed great potential for obtaining canopy height and aboveground biomass by using UAV at a large plot scale (Figure 13). Most vegetation height could be inverted with reasonable values, except for that located at the edge of the orthophotoquad which could not be accurately retrieved due to the limited UAV photos (Figure 13b). As also shown in Figure 13, the *Spartina alterniflora* of this area was patchy in spatial distribution, and vegetation height at the edge of the patch was relatively lower than in the inner area of the patch. The vegetation height map retrieved by UAV reflected the spatial distribution of *Spartina alterniflora*. In addition, the vegetation height spatial distribution pattern with coarse resolution (Figure 13c) was consistent with that of high resolution (Figure 13b), which provided a guarantee for accurate estimation of aboveground biomass at a large plot scale (Figure 13d). These preliminary application results indicated that our constructed estimation model could also be used to estimate aboveground biomass at a plot scale, which was useful for estimating the aboveground biomass at a satellite pixel-scale level in the future.

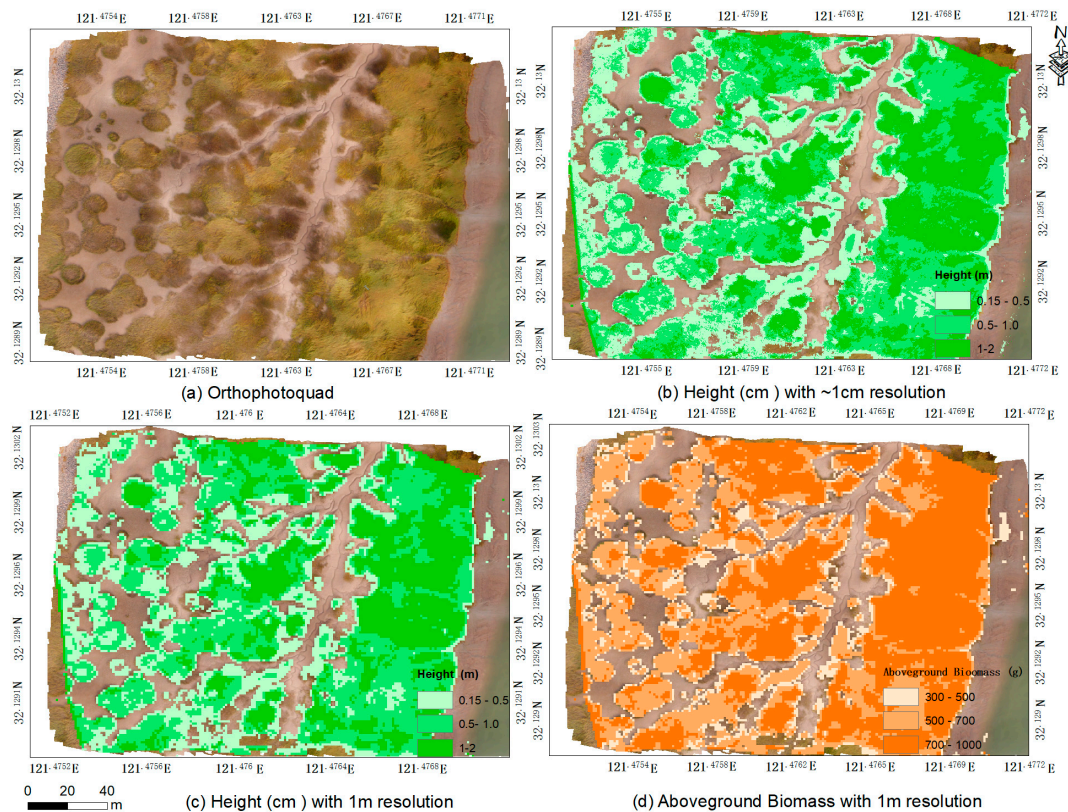


**Figure 13.** The UAV orthophotoquad image of the spatial distribution of *Spartina alterniflora* in the Jiangsu study site (a); the height distribution map with ~1 cm resolution (b); the resampling height distribution map with 1 m resolution (c); and the inversed aboveground biomass distribution map (d).

#### 4.6. Limitations and Future Research

In this study, we only used vegetation height to estimate vegetation aboveground biomass without considering the grassland type. However, the aboveground biomass estimation error analysis results (Figure 12) indicated a slight variance in UAV performance accuracy in the different grassland types. For example, the dominant vegetation type observed in the Inner Mongolia study site was desert steppe, and the rRMSE of predicted aboveground biomass was relatively higher than the other two sites (Table 5). Therefore, we will increase the number of study sites and samples of different vegetation types to further verify the feasibility of UAV to inverse the height and aboveground biomass of grassland at quadrat scale in future studies.

Though our results confirmed the feasibility of UAV inversion of grassland canopy height and aboveground biomass at quadrat scale, the use of the constructed aboveground biomass estimation model in other sites still needed validation.

Even though the 1 m<sup>2</sup> quadrat scale estimation model had been applied to estimate the grassland aboveground biomass at a plot scale, further investigation is needed to determine the best method for scaling up the parameters obtained from UAV to the commonly used satellites, such as Sentinel-2, Landsat, or MODIS data. In addition, the relationships between aboveground biomass and satellite spectral indices at the same scale should be established and tested before regional application.

## 5. Conclusions

In this study, synchronous experiments of UAV and field sampling were conducted at three study sites to explore the feasibility of inverting the canopy height and aboveground biomass of grassland at quadrat scale from UAV images.

Based on the acquired UAV images, point clouds and CHM metrics of each quadrat were calculated by using SfM and CHM algorithms to explore the relationships between CHM metrics and field measurements. CHM\_mean was the most suitable variable to estimate the canopy height and biomass of grassland at quadrat scale. Our results confirmed that UAV could be used to estimate grassland vegetation height and aboveground biomass of grassland at quadrat scale.

In addition, we also estimated the grassland aboveground biomass at a large plot scale by joint use of the constructed estimation model and UAV at the Jiangsu study site. It indicated that the 1 m<sup>2</sup> quadrat scale model could be well used to invert canopy height and aboveground biomass at a large plot scale. It showed great potential for estimating aboveground biomass of grassland at a satellite pixel-scale, which is significantly useful for resolving the issues of scale mismatching when retrieving aboveground biomass from remote sensing at the regional or global scale.

**Author Contributions:** S.Y. conceived and designed the experiments; H.Z., Y.S., L.C., Y.Q. (Yu Qin), J.C. and Y.Q. (Yan Qin) performed the experiments; J.D. contributed analysis tools; All authors contributed to the interpretation of the results and the writing of the paper.

**Acknowledgments:** We would like to thank Zhihua Zhang for helping field data collection; and Wenda Cao for helping with UAV data processing. This work was funded by grants from the National Key R&D Program of China (2017YFA0604801), the National Natural Science Foundation Commission (41690142), the Nantong Key Laboratory project (CP12016005) and the Opening Foundation of the State Key Laboratory Breeding Base of Desertification and Aeolian Sand Disaster Combating, Gansu Desert Control Research Institute (GSDC201504).

**Conflicts of Interest:** The authors declare no conflict of interest.

## References

1. Scurlock, J.M.O.; Hall, D.O. The global carbon sink: A grassland perspective. *Glob. Chang. Biol.* **1998**, *4*, 229–233. [[CrossRef](#)]
2. Hoekstra, J.; Boucher, T.; Ricketts, T.; Roberts, C. Confronting a biome crisis: Global disparities of habitat loss and protection. *Ecol. Lett.* **2005**, *8*, 23–29. [[CrossRef](#)]
3. Bai, Y.; Han, X.; Wu, J.; Chen, Z.; Li, L. Ecosystem stability and compensatory effects in the inner Mongolia grassland. *Nature* **2004**, *431*, 181–184. [[CrossRef](#)] [[PubMed](#)]
4. Chen, Z.; Zhang, X. Value of ecosystem services in China. *Sci. Bull.* **2000**, *45*, 870–876. [[CrossRef](#)]
5. Hall, D.O.; Scurlock, J.M.O. Climate change and productivity of natural grasslands. *Ann. Bot.* **1991**, *67*, 49–55. [[CrossRef](#)]
6. Scurlock, J.M.O.; Johnson, K.; Olson, R.J. Estimating net primary productivity from grassland biomass dynamics measurements. *Glob. Chang. Biol.* **2002**, *8*, 736–753. [[CrossRef](#)]
7. Parton, W.J.; Scurlock, J.M.O.; Ojima, D.S.; Schimel, D.S.; Hall, D.O.; Members, S.G. Impact of climate change on grassland production and soil carbon worldwide. *Glob. Chang. Biol.* **1995**, *1*, 13–22. [[CrossRef](#)]
8. Piao, S.; Fang, J.; Zhou, L.; Tan, K.; Tao, S. Changes in biomass carbon stocks in China's grasslands between 1982 and 1999. *Glob. Biogeochem. Cycles* **2007**, *21*. [[CrossRef](#)]
9. Qian, S.; Fu, Y.; Pan, F.F. Climate change tendency and grassland vegetation response during the growth season in three-river source region. *Sci. China Earth Sci.* **2010**, *53*, 1506–1512. [[CrossRef](#)]
10. Guo, Q.; Hu, Z.; Li, S.; Li, X.; Sun, X.; Yu, G. Spatial variations in aboveground net primary productivity along a climate gradient in Eurasian temperate grassland: Effects of mean annual precipitation and its seasonal distribution. *Glob. Chang. Biol.* **2012**, *18*, 3624–3631. [[CrossRef](#)]
11. Townsend, K.J. *Measurement of Grassland Biomass in South-Central Florida Using Data from Ikonos and Landsat 7 Satellites*; FAO: Rome, Italy, 2001.
12. Xie, Y.; Sha, Z.; Mei, Y.; Bai, Y.; Lei, Z. A comparison of two models with Landsat data for estimating above ground grassland biomass in inner Mongolia, China. *Ecol. Model.* **2009**, *220*, 1810–1818. [[CrossRef](#)]
13. Friedl, M.A.; Schimel, D.S.; Michaelsen, J.; Davis, F.W.; Walker, H. Estimating grassland biomass and leaf area index using ground and satellite data. *Int. J. Remote Sens.* **1994**, *15*, 1401–1420. [[CrossRef](#)]
14. Niu, Z.; Ni, S. Study on models for monitoring of grassland biomass around Qinghai lake assisted by remote sensing. *Acta Geogr. Sin.* **2003**, *58*, 695–702.
15. Liu, Y.; Zha, Y.; Gao, J.; Ni, S. Assessment of grassland degradation near lake Qinghai, west china, using Landsat TM and reflectance spectra data. *Int. J. Remote Sens.* **2004**, *25*, 4177–4189.

16. Dusseux, P.; Hubert-Moy, L.; Corpetti, T.; Vertès, F. Evaluation of spot imagery for the estimation of grassland biomass. *Int. J. Appl. Earth Obs. Geoinf.* **2015**, *38*, 72–77. [[CrossRef](#)]
17. Verbesselt, J.; Somers, B.; van Aardt, J.A.N.; Jonckheere, I.; Coppin, P. Monitoring herbaceous biomass and water content with spot vegetation time-series to improve fire risk assessment in savanna ecosystems. *Remote Sens. Environ.* **2006**, *101*, 399–414.
18. Liu, S.; Su, X.; Dong, S.; Cheng, F.; Zhao, H.; Wu, X.; Zhang, X.; Li, J. Modeling aboveground biomass of an alpine desert grassland with SPOT-VGT NDVI. *Mapp. Sci. Remote Sens.* **2015**, *52*, 680–699. [[CrossRef](#)]
19. Lumbierres, M.; Méndez, P.; Bustamante, J.; Soriguer, R.; Santamaría, L. Modeling biomass production in seasonal wetlands using MODIS NDVI land surface phenology. *Remote Sens.* **2017**, *9*, 392. [[CrossRef](#)]
20. Gao, T.; Xu, B.; Yang, X.; Jin, Y.; Ma, H.; Li, J.; Yu, H. Using MODIS time series data to estimate aboveground biomass and its spatio-temporal variation in inner Mongolia's grassland between 2001 and 2011. *Int. J. Remote Sens.* **2013**, *34*, 7796–7810. [[CrossRef](#)]
21. Kawamura, K.; Akiyama, T.; Yokota, H.O.; Tsutsumi, M.; Yasuda, T.; Watanabe, O.; Wang, S. Comparing MODIS vegetation indices with AVHRR NDVI for monitoring the forage quantity and quality in inner Mongolia grassland, China. *Grassland Sci.* **2005**, *51*, 33–40. [[CrossRef](#)]
22. Zhang, B.; Zhang, L.; Xie, D.; Yin, X.; Liu, C.; Liu, G. Application of synthetic NDVI time series blended from Landsat and MODIS data for grassland biomass estimation. *Remote Sens.* **2016**, *8*, 10. [[CrossRef](#)]
23. Jin, Y.; Yang, X.; Qiu, J.; Li, J.; Gao, T.; Wu, Q.; Zhao, F.; Ma, H.; Yu, H.; Xu, B. Remote sensing-based biomass estimation and its spatio-temporal variations in temperate grassland, northern China. *Remote Sens.* **2014**, *6*, 1496–1513. [[CrossRef](#)]
24. Yang, Y.H.; Fang, J.Y.; Pan, Y.D.; Ji, C.J. Aboveground biomass in Tibetan grasslands. *J. Arid Environ.* **2009**, *73*, 91–95. [[CrossRef](#)]
25. Cho, M.A.; Skidmore, A.K. Hyperspectral predictors for monitoring biomass production in mediterranean mountain grasslands: Majella national park, Italy. *Int. J. Remote Sens.* **2009**, *30*, 499–515. [[CrossRef](#)]
26. Psomas, A.; Kneubühler, M.; Huber, S.; Itten, K.; Zimmermann, N.E. Hyperspectral remote sensing for estimating aboveground biomass and for exploring species richness patterns of grassland habitats. *Int. J. Remote Sens.* **2011**, *32*, 9007–9031. [[CrossRef](#)]
27. Catchpole, W.R.; Wheeler, C.J. Estimating plant biomass: A review of techniques. *Austral Ecol.* **1992**, *17*, 121–131. [[CrossRef](#)]
28. Tucker, C.J. A critical review of remote sensing and other methods for non-destructive estimation of standing crop biomass. *Grass Forage Sci.* **1980**, *35*, 177–182. [[CrossRef](#)]
29. Possoch, M.; Bieker, S.; Hoffmeister, D.; Bolten, A.; Schellberg, J.; Bareth, G. Multi-temporal crop surface models combined with the RGB vegetation index from UAV-based images for forage monitoring in grassland. *Int. Arch. Photogramm. Remote Sens. Spat. Inf. Sci.* **2016**, *41*, 991–998.
30. Gnyp, M.L.; Bareth, G.; Li, F.; Lenz-Wiedemann, V.I.S.; Koppe, W.; Miao, Y.; Hennig, S.D.; Jia, L.; Laudien, R.; Chen, X. Development and implementation of a multiscale biomass model using hyperspectral vegetation indices for winter wheat in the north china plain. *Int. J. Appl. Earth Obs. Geoinf.* **2014**, *33*, 232–242. [[CrossRef](#)]
31. Gnyp, M.L.; Miao, Y.; Yuan, F.; Ustin, S.L.; Yu, K.; Yao, Y.; Huang, S.; Bareth, G. Hyperspectral canopy sensing of paddy rice aboveground biomass at different growth stages. *Field Crops Res.* **2014**, *155*, 42–55. [[CrossRef](#)]
32. Barrachina, M.; Cristóbal, J.; Tulla, A.F. Estimating above-ground biomass on mountain meadows and pastures through remote sensing. *Int. J. Appl. Earth Obs. Geoinf.* **2015**, *38*, 184–192. [[CrossRef](#)]
33. Ullah, S.; Si, Y.; Schlerf, M.; Skidmore, A.K.; Shafique, M.; Iqbal, A. Estimation of grassland biomass and nitrogen using MERIS data. *Int. J. Appl. Earth Obs. Geoinf.* **2012**, *19*, 196–204. [[CrossRef](#)]
34. Mutanga, O.; Adam, E.; Cho, M.A. High density biomass estimation for wetland vegetation using worldview-2 imagery and random forest regression algorithm. *Int. J. Appl. Earth Obs. Geoinf.* **2012**, *18*, 399–406. [[CrossRef](#)]
35. Yang, S.; Feng, Q.; Liang, T.; Liu, B.; Zhang, W.; Xie, H. Modeling grassland above-ground biomass based on artificial neural network and remote sensing in the three-river headwaters region. *Remote Sens. Environ.* **2017**, *204*, 448–455. [[CrossRef](#)]
36. Li, F.; Zeng, Y.; Luo, J.; Ma, R.; Wu, B. Modeling grassland aboveground biomass using a pure vegetation index. *Ecol. Indic.* **2016**, *62*, 279–288. [[CrossRef](#)]

37. Bendig, J.; Bolten, A.; Bennertz, S.; Broscheit, J.; Eichfuss, S.; Bareth, G. Estimating biomass of barley using crop surface models (CSMS) derived from UAV-based RGB imaging. *Remote Sens.* **2014**, *6*, 10395–10412. [[CrossRef](#)]
38. Bendig, J.; Yu, K.; Aasen, H.; Bolten, A.; Bennertz, S.; Broscheit, J.; Gnyp, M.L.; Bareth, G. Combining UAV-based plant height from crop surface models, visible, and near infrared vegetation indices for biomass monitoring in barley. *Int. J. Appl. Earth Obs. Geoinf.* **2015**, *39*, 79–87. [[CrossRef](#)]
39. Pölönen, I.; Saari, H.; Kaivosoja, J.; Honkavaara, E.; Pesonen, L. Hyperspectral imaging based biomass and nitrogen content estimations from light-weight UAV. *SPIE Remote Sens.* **2013**, *8887*, 521–525.
40. Wallace, L.; Lucieer, A.; Watson, C.; Turner, D. Development of a UAV-lidar system with application to forest inventory. *Remote Sens.* **2012**, *4*, 1519–1543. [[CrossRef](#)]
41. Wallace, L.; Lucieer, A.; Watson, C.S. Evaluating tree detection and segmentation routines on very high resolution UAV lidar data. *IEEE Trans. Geosci. Remote Sens.* **2014**, *52*, 7619–7628. [[CrossRef](#)]
42. Tilly, A.N.; Hoffmeister, D.; Cao, Q.; Huang, S.; Lenz-Wiedemann, V.; Miao, Y.; Bareth, G. Multitemporal crop surface models: Accurate plant height measurement and biomass estimation with terrestrial laser scanning in paddy rice. *J. Appl. Remote Sens.* **2014**, *8*, 083671. [[CrossRef](#)]
43. Cooper, S.; Roy, D.; Schaaf, C.; Paynter, I. Examination of the potential of terrestrial laser scanning and structure-from-motion photogrammetry for rapid nondestructive field measurement of grass biomass. *Remote Sens.* **2017**, *9*, 531. [[CrossRef](#)]
44. Wang, D.; Xin, X.; Shao, Q.; Brolly, M.; Zhu, Z.; Chen, J. Modeling aboveground biomass in hulunber grassland ecosystem by using unmanned aerial vehicle discrete lidar. *Sensors* **2017**, *17*, 180. [[CrossRef](#)] [[PubMed](#)]
45. Li, W.; Niu, Z.; Chen, H.; Li, D.; Wu, M.; Zhao, W. Remote estimation of canopy height and aboveground biomass of maize using high-resolution stereo images from a low-cost unmanned aerial vehicle system. *Ecol. Indic.* **2016**, *67*, 637–648. [[CrossRef](#)]
46. Souza, C.H.W.D.; Lamparelli, R.A.C.; Rocha, J.V. Height estimation of sugarcane using an unmanned aerial system UAS based on structure from motion SFM point clouds. *Int. J. Remote Sens.* **2017**, *38*, 2218–2230. [[CrossRef](#)]
47. Snavely, N.; Seitz, S.M.; Szeliski, R. Modeling the world from internet photo collections. *Int. J. Comput. Vis.* **2008**, *80*, 189–210. [[CrossRef](#)]
48. St-Onge, B.A.; Achaichia, N. Measuring forest canopy height using a combination of lidar and aerial photography data. *Int. Arch. Photogramm. Remote Sens.* **2001**, *34*, 131–137.
49. Popescu, S.C. Estimating biomass of individual pine trees using airborne lidar. *Biomass Bioenergy* **2007**, *31*, 646–655. [[CrossRef](#)]
50. Wallace, L.; Lucieer, A.; Malenovský, Z.; Turner, D.; Vopěnka, P. Assessment of forest structure using two UAV techniques: A comparison of airborne laser scanning and structure from motion (SFM) point clouds. *Forests* **2016**, *2016*, 62. [[CrossRef](#)]
51. Fraser, R.; Olthof, I.; Lantz, T.C.; Schmitt, M.C. UAV photogrammetry for mapping vegetation in the low-arctic. *Arct. Sci.* **2016**, *2*, 79–102. [[CrossRef](#)]
52. Cunliffe, A.M.; Brazier, R.E.; Anderson, K. Ultra-fine grain landscape-scale quantification of dryland vegetation structure with drone-acquired structure-from-motion photogrammetry. *Remote Sens. Environ.* **2016**, *183*, 129–143. [[CrossRef](#)]
53. Schirrmann, M.; Hamdorf, A.; Giebel, A.; Gleiniger, F.; Pflanz, M.; Dammer, K.H. Regression kriging for improving crop height models fusing ultra-sonic sensing with UAV imagery. *Remote Sens.* **2017**, *9*, 665. [[CrossRef](#)]
54. Lussem, U.; Hollberg, J.; Menne, J.; Schellberg, J.; Bareth, G. Using calibrated RGB imagery from low-cost uavs for grassland monitoring: Case study at the rengen grassland experiment (RGE), Germany. *Int. Arch. Photogramm. Remote Sens. Spat. Inf. Sci.* **2017**, *42*, 229–233. [[CrossRef](#)]
55. Jing, R.; Gong, Z.; Zhao, W.; Pu, R.; Deng, L. Above-bottom biomass retrieval of aquatic plants with regression models and SFM data acquired by a UAV platform—A case study in wild duck lake wetland, Beijing, China. *ISPRS J. Photogramm. Remote Sens.* **2017**, *134*, 122–134. [[CrossRef](#)]
56. Ma, M.; Zhou, X.; Du, G. Effects of disturbance intensity on seasonal dynamics of alpine meadow soil seed banks on the Tibetan plateau. *Plant Soil* **2013**, *369*, 283–295. [[CrossRef](#)]

57. Yi, S. FragMAP: A tool for long-term and cooperative monitoring and analysis of small-scale habitat fragmentation using an unmanned aerial vehicle. *Int. J. Remote Sens.* **2017**, *38*, 2686–2697. [CrossRef]
58. Yi, S.; Chen, J.; Qin, Y.; Xu, G. The burying and grazing effects of plateau PIKA on alpine grassland are small: A pilot study in a semiarid basin on the Qinghai-Tibet plateau. *Biogeosciences* **2016**, *13*, 6273–6284. [CrossRef]
59. Qin, Y.; Yi, S.; Ding, Y.; Xu, G.; Chen, J.; Wang, Z. Effects of small-scale patchiness of alpine grassland on ecosystem carbon and nitrogen accumulation and estimation in northeastern Qinghai-Tibetan plateau. *Geoderma* **2018**, *318*, 52–63. [CrossRef]
60. Nex, F.; Remondino, F. UAV for 3D mapping applications: A review. *Appl. Geomat.* **2014**, *6*, 1–15. [CrossRef]
61. Sona, G.; Pinto, L.; Pagliari, D.; Passoni, D.; Gini, R. Experimental analysis of different software packages for orientation and digital surface modelling from UAV images. *Earth Sci. Inform.* **2014**, *7*, 97–107. [CrossRef]
62. Agisoft. *Agisoft Photoscan User Manual: Professional Edition*, Version 1.3; Agisoft: St. Petersburg, Russia, 2017.
63. CloudCompare. *CloudCompare Version 2.6.1 User Manual*; CloudCompare. Available online: <http://www.cloudcompare.org/doc/qCC/CloudCompare%20v2.6.1%20-%20User%20manual.pdf> (accessed on 20 May 2018).
64. Woebbecke, D.; Meyer, G.; Von Bargen, K.; Mortensen, D. Color indices for weed identification under various soil, residue, and lighting conditions. *Trans. ASAE* **1995**, *38*, 259–269. [CrossRef]
65. Bareth, G.; Bendig, J.; Tilly, N.; Hoffmeister, D.; Aasen, H.; Bolten, A. A comparison of UAV- and TLS-derived plant height for crop monitoring: Using polygon grids for the analysis of crop surface models (CSMS). *Photogramm. Fernerkund. Geoinf.* **2016**, *2016*, 85–94. [CrossRef]
66. Lussem, U.; Bareth, G. *Introducing a New Concept for Grassland Monitoring: The Multi-Temporal Grassland Index (MtGI)*; 38th Scientific-Technical Annual Meeting of the DGPF and PFGK18 Conference in Munich—Publications of the DGPF; 2018; Volume 27, pp. 285–293. Available online: [https://www.dgpf.de/src/tagung/jt2018/proceedings/proceedings/papers/97\\_PFGK18\\_Lussem\\_Bareth.pdf](https://www.dgpf.de/src/tagung/jt2018/proceedings/proceedings/papers/97_PFGK18_Lussem_Bareth.pdf) (accessed on 20 May 2018).
67. Zahawi, R.A.; Dandois, J.P.; Holl, K.D.; Nadwodny, D.; Reid, J.L.; Ellis, E.C. Using lightweight unmanned aerial vehicles to monitor tropical forest recovery. *Biol. Conserv.* **2015**, *186*, 287–295. [CrossRef]
68. Hopkinson, C.; Chasmer, L.E.; Sass, G.; Creed, I.F.; Sitar, M.; Kalbfleisch, W.; Treitz, P. Vegetation class dependent errors in lidar ground elevation and canopy height estimates in a boreal wetland environment. *Can. J. Remote Sens.* **2005**, *31*, 191–206. [CrossRef]
69. Wang, C.; Menenti, M.; Stoll, M.P.; Feola, A.; Belluco, E.; Marani, M. Separation of ground and low vegetation signatures in lidar measurements of salt-marsh environments. *IEEE Trans. Geosci. Remote Sens.* **2009**, *47*, 2014–2023. [CrossRef]
70. Xia, J.; Ma, M.; Liang, T.; Wu, C.; Yang, Y.; Zhang, L.; Zhang, Y.; Yuan, W. Estimates of grassland biomass and turnover time on the Tibetan plateau. *Environ. Res. Lett.* **2017**, *13*, 014020. [CrossRef]



© 2018 by the authors. Licensee MDPI, Basel, Switzerland. This article is an open access article distributed under the terms and conditions of the Creative Commons Attribution (CC BY) license (<http://creativecommons.org/licenses/by/4.0/>).